# Analysis of two-prong events in $pp$ interactions at 205 GeV/$c$: Separation of elastic and inelastic events*

S. Barish, D. Colley,† M. Derrick, B. Musgrave,
P. Schreiner, and H. Yuta
*Argonne National Laboratory, Argonne, Illinois 60439*

(Received 23 October 1973)

We present results of complete measurements of the two-prong events observed in a 50 000-picture exposure of the 30-in. hydrogen bubble chamber to a 205-GeV/$c$ proton beam at the National Accelerator Laboratory. Using kinematic fitting, elastic and inelastic events are separated and cross sections are obtained. The total two-prong cross section is measured to be $9.77 \pm 0.40$ mb, of which $2.85 \pm 0.26$ mb represents the inelastic contribution. The total elastic cross section is measured to be $6.92 \pm 0.44$ mb. Our data are consistent with the break in $d\sigma/dt$ at $|t| \sim 0.1$–$0.2$ (GeV/$c$)$^2$ observed at the CERN ISR. A prominent low-mass enhancement is observed in the distribution of missing mass squared from the slow proton for the inelastic events. An analysis based on the missing-mass spectrum and the particle rapidities shows that this low-mass enhancement accounts for about 77% of the total inelastic two-prong cross section. The diffractive cross section in the two-prong events is $2.20 \pm 0.25$ mb, in agreement with certain two-component models.

## I. INTRODUCTION

Experiments at both the CERN ISR and the National Accelerator Laboratory (NAL)[1] have measured diffractive excitation of the proton, seen as a broad, low-mass enhancement (up to ~7 GeV) in the missing-mass spectrum produced peripherally from the target or projectile. The interpretation of this result as single diffractive dissociation of the proton rests on the observation that the differential cross section is approximately constant in shape and magnitude over a wide energy range and is about equal to that for elastic $pp$ scattering. Bubble-chamber experiments show that the process occurs predominantly in the low-multiplicity final states, as it is observed in the two-, four-, and six-charged prong topologies, but so far not in the higher multiplicities.[2,3] As seen in the 205-GeV data, the contribution to this enhancement from the two-prong events peaks at a lower mass than is the case for the four- and six-prong events, although the exact shape of the two-prong peak depends somewhat on a clean separation of the elastic and inelastic events, which is a principal subject of this paper.

The shape of the differential cross section for elastic scattering at high energy is also interesting in view of the data obtained at the ISR showing a marked change in slope near $t = -0.10$ (GeV/$c$)$^2$.[4] In addition, the observation of a rise in the elastic cross section with energy[5] makes a measurement of of the absolute value of the elastic cross section important.

We have studied the two-prong reactions

$$pp \to p + p\,, \tag{1}$$

$$pp \to p + X^+ + \cdots\,, \tag{2}$$

$$pp \to \pi^+ + X^+ + \cdots\,, \tag{3}$$

$$pp \to p + \pi^+ + \cdots\,, \tag{4}$$

$$pp \to X^+ + X^+ + \cdots\,, \tag{5}$$

where $p$ and $\pi^+$ in reactions (2), (3), and (4) are protons and $\pi^+$'s identified by ionization density, and $X^+$ represents the unidentifiable positively charged particle.

## II. EXPERIMENTAL DETAILS

The data come from the measurement of two-prong events observed in a 50 000-picture exposure of the 30-in. hydrogen bubble chamber to a 205-GeV/$c$ proton beam at NAL. Previous results from this exposure have been given in several publications.[6] From a scan of the entire film sample, 1969 two-prong events were found in a fiducial volume defined on a scan table. The scanning efficiency was $(98 \pm 2)\%$ for the events found, excluding those lost at small values of recoil proton momentum. The events were measured on POLLY III[7] and processed through the reconstruction program TVGP. Events which failed to give satisfactory reconstruction were measured on a film-plane digitizer with up to four measurement passes where necessary. About 95% of the total two-prong events gave a successful geometrical reconstruction.

Most of the unsuccessful measurements are on events with another interaction near the vertex

or an adjacent beam track, so we believe that the 5% of the events which are unsuccessful do not cause any systematic bias. For the successful events, we used ionization information to identify outgoing tracks with laboratory momentum less than 1.5 GeV/$c$. In about 95% of the successfully measured two-prong events, it was possible to identify at least one charged secondary as a $\pi^+$ or proton from the observed ionization density. No correction is applied for the small number of $K^+$ misidentified as $\pi^+$ or $p$, although we did observe one event with a $K^+$ unambiguously identified by ionization.

## III. SEPARATION OF ELASTIC AND INELASTIC EVENTS

To select the elastic events, kinematic fitting in the program SQUAW was used. Selection using individual kinematic constraints such as coplanarity, the missing mass from the recoil proton, and the scattering angle between the target and the recoil proton was not adequate to achieve the elastic-inelastic separation. This is because the individual measurement errors on the high-energy tracks in the 30-in. chamber are too large for the simple methods to be reliable.[7] The complete kinematic fit was adequate, however, as we will discuss, and the measurement errors were determined by imposing the requirement that the stretch functions from SQUAW for the elastic fits have unit rms width.

The beam momentum was fixed at the design value of 205 GeV/$c$, and we assigned an uncertainty of ±2 GeV/$c$. The beam track angles were determined from measurements of noninteracting tracks in the bubble chamber. In order to avoid using momentum measurements of high-momentum tracks with large momentum errors, we required that if (1) the momentum of an outgoing track was greater than 10 GeV/$c$ and (2) the percentage error in measured momentum was greater than 5%, the magnitude of the measured momentum was not used. For each such track in a two-prong event, the number of constraints in the fit to reaction (1) was reduced by one.

To improve the fit quality without introducing any bias into the sample, we imposed the following restrictions on the data sample: (1) The interaction vertex must be within a box 44 cm long in the beam direction, 18 cm wide, and 9 cm deep; (2) the film rms deviation of measured track points must be less than $[(30)^2+(2\sigma_C)^2]^{1/2}$ (in microns), where $\sigma_C$ is the expected rms deviation due to Coulomb scattering. After we impose these cuts, 1758 events remain.

The final selection of elastic events was made using the $\chi^2$ distribution for the events that gave an elastic fit and have both outgoing tracks consistent with ionization density for a proton[8]; this distribution is shown in Fig. 1. More than 98% of the events selected as elastic gave 3C fits, and the remainder gave 2C or 4C fits.

We have investigated possible loss from, and also contamination in, the selected elastic sample as a function of $\chi^2$, which, in turn, would affect the inelastic sample. To study the loss of elastic events, we randomly selected 40 events classified as elastic and measured each one eight times. Applying the same restrictions on this sample, we selected the elastic events as a function of $\chi^2$ and found that the fractional loss of elastic events was $0.040\pm0.011$ for $\chi^2<32$, $0.064\pm0.015$ for $\chi^2<24$, and $0.096\pm0.018$ for $\chi^2<18$. We also found that this fractional loss is not correlated with the missing mass squared at our statistical level.

Figures 2(a) and 2(b) show the distribution of missing mass squared, $MM^2=(P_b+P_t-P_s)^2$, for the elastic events selected with $\chi^2<24$ for a 3C fit, and for the inelastic events with an identified proton.[9] Here $P_b$, $P_t$, and $P_s$ are, respectively, the four-momenta of the incident, target, and slow protons. We note that the peak position for the inelastic events is about 0.3 GeV$^2$ higher than that for the elastic events. For comparison, the unshaded histogram in Fig. 2(c) shows the $MM^2$ distribution for the four-prong events with an identified proton,[10] in which the peak position is still higher than that for the inelastic two-prong events.

The contamination in the elastic events will often arise from events with one or more neutral pions. To study this contamination, we used measurements of the four-prong events and fitted each

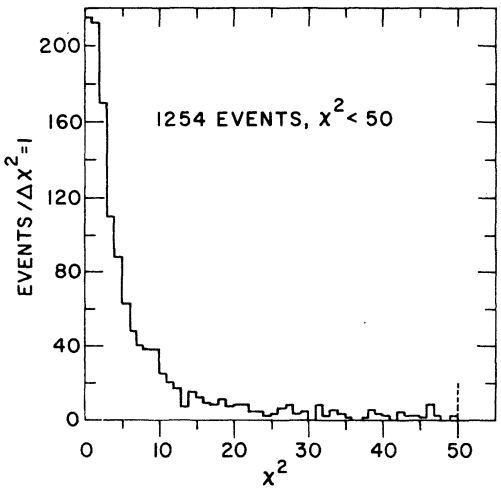


FIG. 1. $\chi^2$ distribution for events that give a fit to $pp$ elastic scattering with $\chi^2<50$.

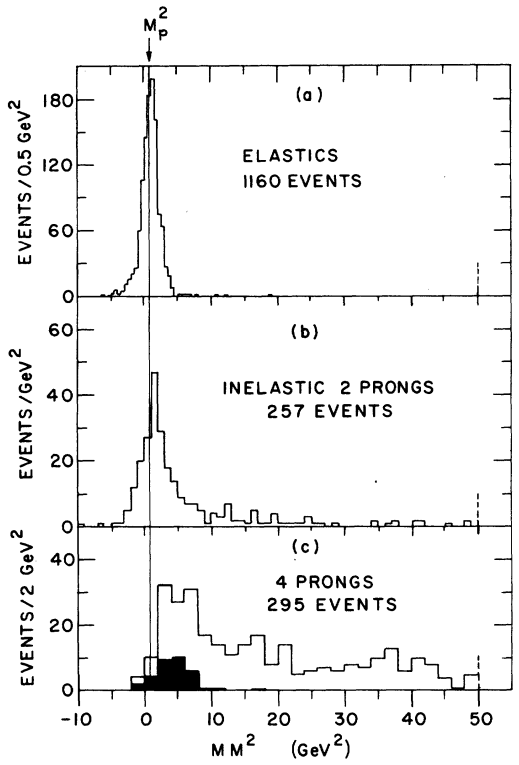


FIG. 2. Missing-mass-squared ($MM^2$) distribution for (a) elastic events selected with $\chi^2 < 24$, (b) two-prong inelastic events with a proton identified by ionization density, and (c) four-prong events with an identified proton. The shaded area in (c) corresponds to those four-prong events that give fits to elastic scattering when the negative track and one of the positive tracks are deleted.

pair of possible proton tracks in turn to hypothesis (1). The shaded histogram in Fig. 2(c) shows the missing-mass-squared distribution for the four-prong events that fit hypothesis (1) with $\chi^2 < 24$,[11] indicating that a substantial number of the inelastic events do give spurious elastic fits. About 75% of the shaded events form a $pp\pi^+\pi^-$ final state,[10] and it is plausible to assume that these events represent a simulation of the $pp\pi^0\pi^0$ contamination in the elastic events. Because of the large errors in $MM^2$ (~1.5 GeV$^2$) and in the angles of fast positive tracks (~2 mrad) in the four-prong events, the events in Fig. 2(c) may also be taken to represent the $pp\pi^0$ final state.

Using the above assumptions, we take the ratio of the shaded to unshaded data in Fig. 2(c) as measuring the variation with $MM^2$ of the percentage of spurious fits, from events with one or more additional $\pi^0$'s. Using data in the shaded and unshaded histograms gives the correction factor, $F(MM^2)$ of Fig. 3(a). Explicitly, $F(MM^2) = 1/(1-f)$, where $f$ is the ratio of the black to the white histogram in Fig. 2(c).

The initially separated inelastic mass spectrum must first have the contamination from the elastic sample subtracted (estimated as 6.4% for the $\chi^2 = 24$ cut), and then be multiplied by $F(MM^2)$ to give the corrected mass spectrum. The smooth curve in Fig. 3(a) has been drawn through the data points with the assumptions that $F(MM^2)$ gives the maximum correction at, and is symmetric about, the proton mass squared.

Figure 3(b) shows the corrected missing-mass distribution for the inelastic events. Compared to Fig. 2(b), the corrected spectrum is suppressed in the region $MM^2 < 2$ GeV$^2$, but is raised slightly in the region $MM^2 > 2$ GeV$^2$. The corrected number of inelastic events with $-5 < MM^2 < 10$ GeV$^2$ is $202 \pm 51$. This can be compared with 203 events in the uncorrected distribution in the same mass region.

We have also calculated the corrected missing-mass spectra for the inelastic events using different $\chi^2$ selections and have found that the shapes of the corrected distributions are quite insensitive to the $\chi^2$ cutoff used. The corrected numbers of events for $-5 < MM^2 < 10$ GeV$^2$ are $196 \pm 50$, $202 \pm 51$, and $253 \pm 63$ for $\chi^2$ cuts at 18, 24, and 32, respectively. The corresponding uncorrected numbers are 241, 203, and 182 events, respectively. Since the selection with a $\chi^2$ cut at 24 gives almost the same numbers for the corrected and uncorrected inelastic events, we finally define the elastic events as those with $\chi^2 < 24$ and the inelastic events as those with $\chi^2 \geq 24$. We estimate contaminations of $(6.3 \pm 0.8)\%$ in the elastic sam-

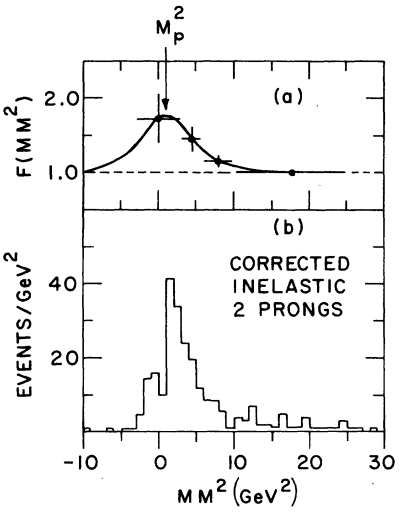


FIG. 3. (a) Correction factor, $F(MM^2)$, for the two-prong inelastic events calculated from the data of Fig. 2(c). (b) The corrected distribution of missing mass squared for the two-prong inelastic events.

TABLE I. Cross sections for elastic and two-prong inelastic channels.

| Reaction | Uncorrected No. of events | Corrected No. of events | Cross section (mb) |
|---|---|---|---|
| $pp \to p + p$ | 1160 | 1449 | $6.92 \pm 0.44$[a] |
| $\to p + X^+ + \cdots$ | 363 | 363 | $1.73 \pm 0.23$ |
| $\to \pi^+ + X^+ + \cdots$ | 153 | 153 | $0.73 \pm 0.07$ |
| $\to p + \pi^+ + \cdots$ | 7 | 7 | $0.03 \pm 0.01$ |
| $\to X^+ + X^+ + \cdots$ | 75 | 75 | $0.36 \pm 0.04$ |
| Total inelastic | 598 | 598 | $2.85 \pm 0.26$[a] |
| Total | 1758 | 2047 | $9.77 \pm 0.40$ |

[a]The errors on the elastic and total inelastic cross sections include the uncertainty coming from the elastic-inelastic separation. This does not apply to the total cross section.

ple and $(36 \pm 5)\%$ in the inelastic sample for $MM^2 < 10\,GeV^2$.

This contamination in the elastic sample (73 events) is consistent with the number of observed associated $e^+e^-$ pairs. We find 18 two-prong events with associated photon conversions, four of which come from the inelastic two-prong events with $MM^2 < 15\,GeV^2$. At most, one photon conversion is associated with the elastic sample. Since the average conversion probability per photon is only 0.018, one photon conversion corresponds to about 30 $\pi^0$'s, which is not inconsistent with the above contamination estimate.

## IV. RESULTS

### A. Cross sections

Table I gives the cross sections for the elastic and two-prong inelastic scattering channels obtained from this experiment using the separation techniques discussed in Sec. III. To calculate the cross sections, we first make a correction for unseen elastic events in the small-momentum-transfer region. We make no azimuthal-loss correction, and we obtain the low-$|t|$ correction by fitting the distribution between 0.04 and 0.16 $(GeV/c)^2$ to the form $Ae^{Bt}$. We have compared the above fit with one for the sample with an azimuthal angle cut applied for all $|t|$ and have found that both fits agree within one standard deviation. We have also compared the ratio of elastic to inelastic events for both cases and have found no significant differences. Using the corrected number of elastic events, the total number of scanned events for all topologies, and a $pp$ total cross section of $(39.0 \pm 1.0)$ mb,[5,12] we obtain a total two-prong cross section of $(9.77 \pm 0.40)$ mb and the channel cross sections given in Table I. For this calculation, we have not made any correction to the inelastic events in the small-$|t|$ region since no loss of events was obvious in this region. From the azimuthal angular distribution in the first bin of the $MM^2 < 10\,GeV^2$ data of Fig. 5, we would expect a maximum correction of 10% to this data point. Since this correction is very uncertain and since the elastic-inelastic separation in that region is least reliable, we do not apply any correction. Allowing for the uncertainty in the estimated loss of elastic events at low $t$, our data sample corresponds to $(4.77 \pm 0.22)$ $\mu$b/event.

Figure 4 shows the $pp$ elastic and inelastic two-

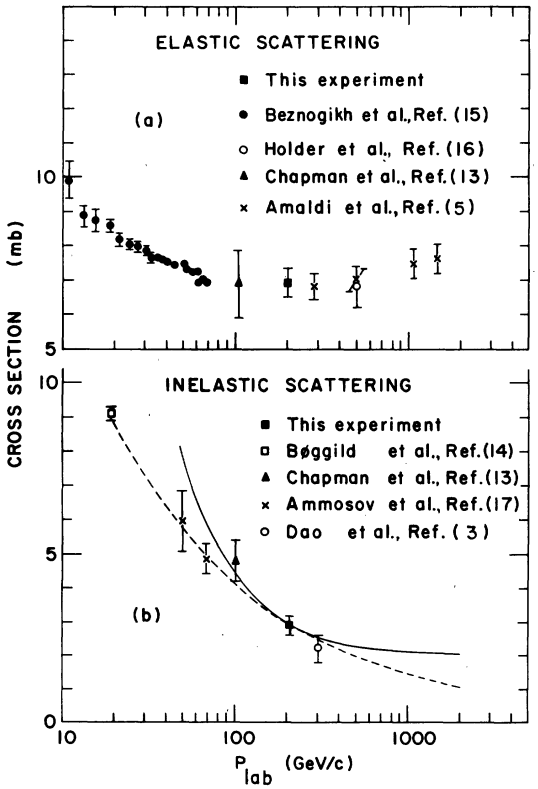


FIG. 4. Total two-prong cross sections as a function of laboratory momentum; (a) $pp$ elastic scattering, (b) $pp$ inelastic scattering. The solid line gives the prediction of the Frazer model, which falls to 2 mb at asymptotic energies, whereas the dashed line represents the best fit to a power law $\sigma \sim P_{lab}^{-0.47}$.

prong cross sections as a function of incident beam momentum.[3,5,13-17] The cross sections obtained from this experiment agree, within errors, with the trend of data from other experiments. We note that the inelastic two-prong cross section decreases with increasing incident momentum, even up to 300 GeV/$c$. Fitting this cross section to the form $P_{\text{lab}}^{-n}$, we obtain $n = 0.47 \pm 0.03$. This energy dependence, shown on Fig. 4(b) as the dashed curve, suggests that a large contribution to the two-prong inelastic process is from non-diffractive processes even at our high energy. The solid curve in Fig. 4(b) is the prediction of the model of Frazer *et al.*[18] This is a two-component model incorporating a multiperipheral contribution and a diffraction component. Our data point is in remarkably good agreement with the predictions of this calculation. One would only expect such a model to apply at very high energies, so the discrepancy between the solid curve and the data points below 100 GeV/$c$ should not be taken seriously.

Figure 5 shows the differential cross sections for elastic and inelastic two-prong scattering. For the inelastic scattering, we have plotted the cross sections separately for events with $MM^2 \leq 10$ GeV$^2$ and for those with $10 < MM^2 \leq 100$ GeV$^2$. Apparently, the elastic differential cross section has a steeper slope than that for inelastic scattering. Since the inelastic events with $MM^2 \leq 10$ GeV$^2$ have an estimated contamination of 36% from the elastic events, the true inelastic slope for this mass region is presumably somewhat less steep than that shown in Fig. 5.

For the elastic events, Table II gives the values of the slope parameter $B$ obtained from fits of the form $d\sigma/dt = Ae^{Bt}$ with the $t$ ranges used for each fit. The fits are also superimposed on the data in Fig. 5. Our data are consistent with a break in slope at momentum transfer between 0.1 and 0.2 (GeV/$c$)$^2$, as first observed by Barbiellini *et al.*[4] at the ISR. Since we do not have enough data to accurately fit the distribution for $|t| < 0.1$ (GeV/$c$)$^2$, we have used the $|t|$ region between 0.04 and 0.16 (GeV/$c$)$^2$ and obtain a slope of (12.1 ±1.2) (GeV/$c$)$^{-2}$, whereas the slope obtained for the

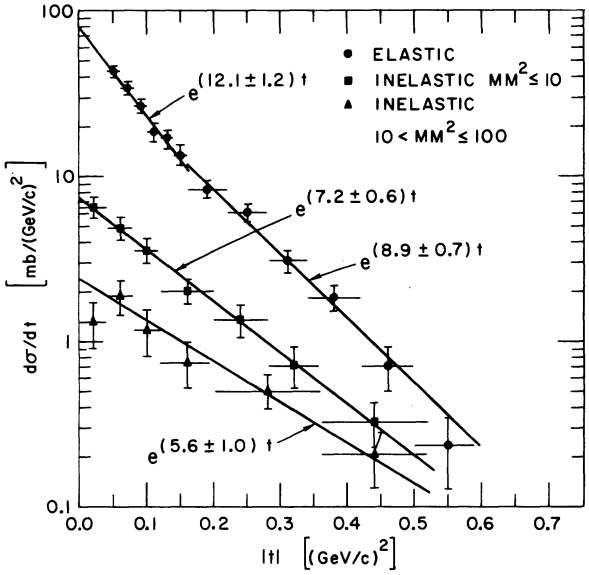


FIG. 5. Measured differential cross sections for elastic events and for two-prong inelastic events with $MM^2 \leq 10$ GeV$^2$ and with $10 < MM^2 \leq 100$ GeV$^2$.

$|t|$ region between 0.16 and 0.6 (GeV/$c$)$^2$ is (8.9 ±0.7) (GeV/$c$)$^{-2}$. These results are consistent with the slopes observed at the CERN ISR,[4,19] at Serpukhov,[20] and at NAL.[21]

We have also fitted the complete distribution for the $|t|$ region between 0.04 and 0.6 (GeV/$c$)$^2$, and find a slope of (9.9 ± 0.4) (GeV/$c$)$^{-2}$ with a $\chi^2$ of 10.1 for 10 degrees of freedom, so although our data are consistent with two slopes, they do not require them. Figure 6 summarizes slope information from all experiments as a function of the square of the total center-of-mass energy, $s$.

Using the extrapolated value obtained from the fit for the $|t|$ region between 0.04 and 0.16 (GeV/$c$)$^2$, we calculate the forward cross section $(d\sigma/dt)_{t=0}$ and find a value of (79.4 ± 8.8) mb/(GeV/$c$)$^2$. Using a total cross section of (39.0 ±1.0) mb, the optical theorem gives the forward cross section

$$\left(\frac{d\sigma}{dt}\right)_{t=0} = \frac{1}{16\pi}\sigma_T^2$$

$$= (77.7 \pm 3.9) \text{ mb/(GeV/}c)^2 .$$

TABLE II. Fits of differential cross sections to the form $Ae^{Bt}$.

| Reaction | $\|t\|$ range [(GeV/$c$)$^2$] | $MM^2$ range (GeV$^2$) | Slope $B$ [(GeV/$c$)$^{-2}$] | $\chi^2$/DF |
|---|---|---|---|---|
| $pp \to p + p$ | 0.04-0.60 | ••• | 9.9 ± 0.4 | 10.1/10 |
| | 0.04-0.16 | ••• | 12.1 ± 1.2 | 1.3/4 |
| | 0.16-0.60 | ••• | 8.9 ± 0.7 | 3.4/4 |
| $pp \to p + X^+ + \cdots$ | 0.0-0.52 | $MM^2 < 10$ | 7.2 ± 0.6 | 0.8/5 |
| | 0.04-0.52 | $10 \leq MM^2 < 100$ | 5.6 ± 1.0 | 0.5/3 |

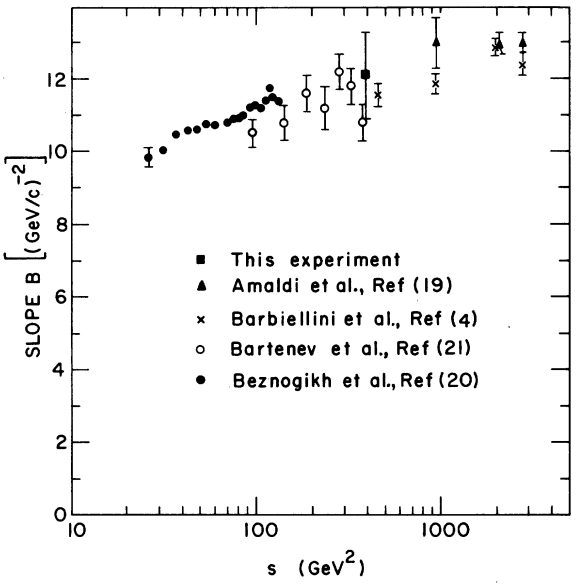


FIG. 6. Slope of forward elastic scattering cross section as a function of $s$. The $t$ ranges used in the different experiments are slightly different, but they are all included between $t = -0.01$ and $t = -0.16$ (GeV/$c$)$^2$.

This gives the square of the ratio of the real to the imaginary amplitudes as $R^2 = 0.02 \pm 0.11$, which is consistent with the more accurate ISR data.[22]

### B. Diffractive component in the inelastic two-prong events

The salient features of the missing-mass distribution of Fig. 2(b) are a pronounced peak at very low mass, $MM^2 < 4$ GeV$^2$, with a tail out to $MM^2 \sim 30$ GeV$^2$. In addition, there is a pedestal extending out to very large $MM^2$. The peak is interpreted as evidence for single inelastic diffractive excitation of, in this case, the beam proton. In order to estimate the single inelastic diffractive cross section, one must define up to what $MM^2$ the diffractively excited states exist and also how to account for any background, for example a multiperipheral background not involving single-Pomeron exchange. Since any definition of diffraction is generally recognized to be rather arbitrary, we use the further information provided by the rapidities of the charged secondaries to estimate the background contribution to the diffractive processes.

The relevant rapidity distributions are shown in Fig. 7. Since the momentum cannot be determined for many fast secondaries and the particle nature is unknown, we use the longitudinal pseudorapidity $\eta = \ln[\tan(\theta/2)]$, where $\theta$ is the laboratory space angle between the secondary particle and the beam track.[23]

Figure 7(a) shows the distribution in $\eta$ for the events classified as elastic scattering. The $\eta$ for the fast forward track can be represented by a Gaussian distribution with $\bar{\eta} = -6.8$ and $\sigma = 0.51$ units. As seen in Table I, the 598 inelastic events are divided into 363 events having a fast particle and an identified proton, 153 events with an identified $\pi^+$, 75 events where both particles were too fast for particle identification, and 7 events where both a proton and a $\pi^+$ could be identified. The distributions in $\eta$ for the above inelastic samples are shown in Figs. 7(b) and 7(e). The peak at $\eta \sim 0$ has in it particles from the target-dissociation sample as well as the recoil protons from the beam-dissociation sample,[24] and vice versa for the peak near $\eta \sim -6$. The shaded area in Fig. 7(b) corresponds to the 75 events with no particle identification.

We note first that the events where neither charged secondary is identified tend to be in the middle but do extend over most of the available

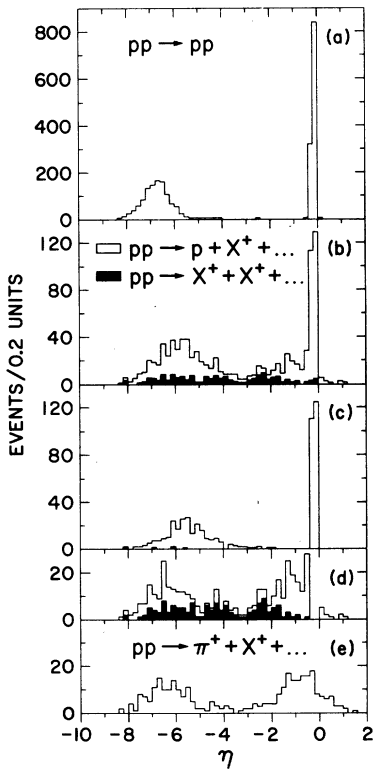


FIG. 7. The rapidity ($\eta$) distribution for (a) the events assigned to elastic scattering; (b) those inelastic events where a proton can be identified (shown as the difference between the black histogram and the white histogram), and the events where neither particle can be identified (shown in the black histogram); (c) a subset of (b) selected to have a slow proton in the elasticlike spike near $\eta = 0$; (d) the remaining events from (b) after subtracting the events in (c); and (e) the events with an identified $\pi^+$.

rapidity space [Fig. 7(b)]. Second, those events with an identified proton show a prominent peak near $\eta = 0$, very similar to the elastic events of Fig. 7(a). This peak corresponds to the recoil proton associated with diffractive dissociation of the beam. For these inelastic events, the spike is superposed on a broadly peaked distribution coming from the dissociation of the target particle.

The broad distribution near $\eta = -6$ for the fast particle in these inelastic events is both shifted and broader than that seen for elastic scattering in Fig. 7(a). Figure 7(c) is a subset of the events in Fig. 7(b) selected to have one particle in the sharp spike near $\eta = 0$ $(0 > \eta > -0.4)$. One notices that the $\eta$ distribution for the fast particles ($\eta \sim -6$) is now even more different from the elastic case than was previously noted for all the data.

Figure 7(d) shows the remaining events of Fig. 7(b) after the above selection. The $\eta$ region $-3.0 \leq \eta \leq 0.0$ contains the particles from target dissociation. Now the $\eta$ distribution for the projectile-fragmentation region ($\sim -4 > \eta > \sim -8$) is similar to that seen in Fig. 7(a), as expected for the protons recoiling from target dissociation. The sharp spike of Fig. 7(b) corresponds to the recoil particles of projectile-fragmentation events and shows that single diffraction is a major contributor to these inelastic events. This observation is in qualitative agreement with the distribution of missing mass squared of Fig. 2(b).

Finally, the events where a $\pi^+$ is identified, Fig. 7(e), show two broad distributions, one due to the slow $\pi^+$ from target dissociation, while the fast-particle distribution is rather similar to those seen in Figs. 7(a) and 7(d). The differences in shape between the $\eta$ distributions for the fast particles in Fig. 7(a) and 7(e) could be the reflection of a possible double-diffraction process.

We now concentrate on the distributions of the rapidity gap between the two charged secondaries shown in Fig. 8. Figure 8(a) shows the distribution for the elastic events. One striking feature of the inelastic data shown in Figs. 8(b) and 8(c) is the appearance of a flat distribution for gaps smaller than about three units of rapidity. From our analysis of the four-charged-particle events in this exposure, we find that although diffractive events are associated with large rapidity gaps, nondiffractive events can have either large or small rapidity gaps.[10] The simple-minded multiperipheral model would also provide a uniform distribution over the whole range of $\Delta\eta$ in Figs. 8(b) and 8(c). We note from Fig. 8(b) that there is a definite nondiffractive component in the two-prong events.

In order to measure this nondiffractive component in the inelastic two-prong sample, we extrapolate the pedestal seen for $\Delta\eta \leq 2$ in Figs. 8(b) and 8(c) under the peak. All events above this background are called diffractive, either single or double. In this way, the diffractive component of the two-prong inelastic cross section is estimated to be $2.20 \pm 0.25$ mb. If, on the other hand, we simply define all events with $|\eta_1 - \eta_2| \geq 3$ as diffractive, we obtain a cross section of $2.45 \pm 0.30$ mb.

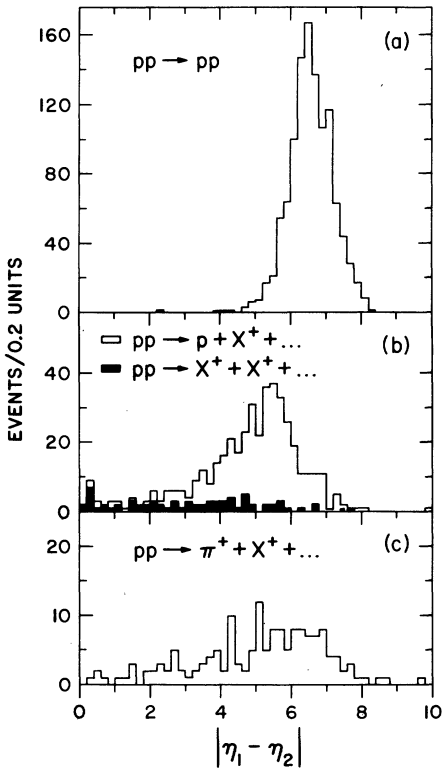


FIG. 8. The distribution of the rapidity gap for the two charged particles for (a) elastic scattering; (b) inelastic events with an identified proton (shown as the difference between the white histogram and the black histogram), and the events where neither particle can be identified (shown as the black histogram); and (c) the events with an identified $\pi^+$.

These estimates can be compared to those obtained using the $MM^2$ distribution of Fig. 2(b). Supposing first that all events with $MM^2 \leq 10$ GeV$^2$ are classified as single inelastic diffraction, we get a cross section of 1.93 mb. Applying factorization, we obtain a double-diffractive component in the two-prong events of 0.14 mb, and so a total diffractive cross section of 2.07 mb. On the other hand, for a lower limit, one might extrapolate a uniform background under the diffractive peak in Fig. 3(b), which is determined by the distribution for 10 GeV$^2 \geq MM^2 \geq 30$ GeV$^2$. This gives a single-diffractive cross section of 1.65 mb to be compared to 1.93 mb obtained previously.

Estimating the nondiffractive background using the $\eta$ representation, we quote as a final conservative value a total diffractive cross section of $2.20 \pm 0.25$ mb. Because of the strong correlation between the elastic-inelastic separation and missing mass, the nondiffractive component has a relatively smaller error and we find a value of $0.65 \pm 0.10$ mb for this process. The two-prong inelastic cross section is then made up of 2.2 mb of diffractive contribution and 0.65 mb of nondiffractive, in agreement with the 2 mb of diffraction predicted by the Frazer model.[18] To establish the validity of this model clearly requires a measurement of the diffractive two-prong cross section at a higher energy than the present experiment. Of the measured 2.2 mb of diffraction, factorization predicts $2.05 \pm 0.22$ mb of single and $0.15 \pm 0.02$ mb of double diffraction. The single-diffractive cross section of $2.05 \pm 0.22$ mb may be compared to the value $2.3 \pm 0.4$ mb measured by Barish *et al.*[2] for the two-prong topology in an analysis of the slow-proton events in the present film.

### C. Charge-exchange processes

In marked contrast to the large cross sections involved in the above diffractive processes, we note that only seven events in the two-prong sample have both a slow $\pi^+$ and a slow proton, corresponding to a charge-exchange process. For all seven events, the $\pi^+ p$ effective mass combination is less than 1.4 GeV, and five of these events are consistent with $\Delta^{++}(1236)$ production. However, only two of these events have a missing mass off the $\pi^+ p$ system, which is consistent with a missing neutron and therefore the reaction

$$pp \to \Delta^{++} n .$$

The low-energy data for this reaction would suggest a cross section of $\sim 3$ $\mu$b at our momentum, assuming a $\sigma \sim P_{\text{lab}}^{-1.9}$ dependence, to be compared to the $(19 \pm 14)$ $\mu$b we observe, corresponding to $\Delta^{++} n$ production in both hemispheres.

## V. CONCLUSIONS

By using kinematic fitting, the observed two-prong events were separated into the elastic and inelastic channels. The data on elastic scattering agree well both with the trend of lower-energy data and with the measurements done at the CERN ISR. The inelastic-scattering cross section is still falling with increasing beam energy. Analysis of the missing-mass distribution and the rapidity distributions shows evidence for a definite nondiffractive component. We estimate that of the $2.85 \pm 0.26$-mb inelastic two-prong cross section, 77% is diffractive. The data are well fitted with the model of Frazer *et al.*, which predicts that diffraction will dominate the two-prong inelastic cross section between 500 and 1000 GeV/$c$. The cross section for $pp \to \Delta^{++} n$ falls on the extrapolation of the cross sections measured at lower energies.

## ACKNOWLEDGMENTS

We acknowledge the efforts of the NAL personnel in providing our exposure. Also, the work of the ANL film analysis staff is appreciated. We have benefited from discussions with R. Arnold, S. Pinsky, G. Thomas, and T. Fields.

---

*Work supported by the U. S. Atomic Energy Commission.

†On leave from the University of Birmingham, Birmingham, England.

[1] *Experiments on High Energy Particle Collisions—1973*, proceedings of the international conference on new results from experiments on high energy particle collisions, Vanderbilt University, 1973 [edited by Robert S. Panvini (A.I.P., New York, 1973)] contains the most recent summary.

[2] S. J. Barish *et al.*, Phys. Rev. Lett. 31, 1080 (1973).

[3] F. T. Dao *et al.*, Phys. Lett. 45B, 399 (1973).

[4] G. Barbiellini *et al.*, Phys. Lett. 39B, 663 (1972).

[5] U. Amaldi *et al.*, Phys. Lett. 44B, 112 (1973).

[6] G. Charlton *et al.*, Phys. Rev. Lett. 29, 515 (1972); 29, 1759 (1972); 30, 574 (1973); Y. Cho *et al.*, *ibid.* 31, 413 (1973).

[7] F. Beck, ANL Report No. ANL/HEP 7128, 1971 (unpublished); F. Beck *et al.*, ANL Report No. ANL-7934, in proceedings of the informal colloquium on POLLY and POLLY-like devices, 1972 (unpublished). The mean space point reconstruction error in a plane perpendicular to the magnetic field is 50 $\mu$. This results in angle errors on 65-cm-long beam tracks of $\Delta\phi = \pm 0.42$ mrad and $\Delta\lambda = \pm 0.63$ mrad, where $\phi$ and $\lambda$ are the azimuthal and dip angles, respectively. The angle error is dominated by measurement errors, and so $\Delta(\phi, \lambda) \propto 1/L$, where $L$ is the length of the track.

[8] There are 160 events with an identified $\pi^+$ (see Table I), of which only two gave elastic fits; these events have been removed from the elastic sample.

[9] The position of the $\chi^2$ cut is arbitrary, but as we discuss later, $\chi^2 = 24$ is the value for which the number of uncorrected and the number of corrected inelastic events are equal.

[10] The data for the four-prong events come from complete measurements of the four-prong events in this exposure; see M. Derrick *et al.*, Phys. Rev. D (to be published).

[11] Since there can be two possible elastic-type fits for each four-prong event, we have taken all fits and

divided by 2 in order to obtain the shaded histogram in Fig. 2(c).

[12]S. R. Amendolia *et al.*, Phys. Lett. 44B, 119 (1973); G. Charlton *et al.*, Phys. Rev. Lett. 29, 515 (1972).
[13]J. W. Chapman *et al.*, Phys. Rev. Lett. 29, 1686 (1972).
[14]H. Bøggild *et al.*, Nucl. Phys. B27, 285 (1971).
[15]G. G. Beznogikh *et al.*, Phys. Lett. 43B, 85 (1973).
[16]M. Holder *et al.*, Phys. Lett. 35B, 361 (1971).
[17]V. V. Ammozov *et al.*, Phys. Lett. 42B, 519 (1972).
[18]W. R. Frazer *et al.*, Phys. Rev. D 7, 2647 (1973).
[19]U. Amaldi *et al.*, Phys. Lett. 36B, 504 (1971).
[20]G. G. Beznogikh, Phys. Lett. 30B, 274 (1969).
[21]V. Bartenev *et al.*, Phys. Rev. Lett. 29, 1755 (1972).
[22]U. Amaldi *et al.*, Phys. Lett. 43B, 231 (1973).
[23]Both Monte Carlo–generated events for particular reactions as well as the real data, where it is possible to check this, indicate that there is little difference, generally less than 0.5 units, between $\eta$ and the real longitudinal rapidity $y = \frac{1}{2}\ln[(E+p_{\parallel})/(E-p_{\parallel})]$.
[24]The different shapes of the data near $\eta = 0$ and near $\eta = -6$ result from the use of the pseudorapidity and the angle errors on the fast forward tracks.

PHYSICAL REVIEW D VOLUME 9, NUMBER 5 1 MARCH 1974

# Systematic study of $\pi^{\pm}p$, $K^{\pm}p$, $pp$, and $\bar{p}p$ forward elastic scattering from 3 to 6 GeV/$c$*

I. Ambats, D. S. Ayres, R. Diebold, A. F. Greene,† S. L. Kramer, A. Lesnik,‡ D. R. Rust,§ C. E. W. Ward, A. B. Wicklund, and D. D. Yovanovitch†
*Argonne National Laboratory, Argonne, Illinois 60439*
(Received 9 August 1973)

Measurements of $\pi^{\pm}p$, $K^{\pm}p$, $pp$, and $\bar{p}p$ elastic scattering are presented for incident momenta of 3, 3.65, 5, and 6 GeV/$c$ and momentum transfers typically 0.03 to 1.8 GeV$^2$. The angle and momentum of the scattered particle were measured with the Argonne Effective Mass Spectrometer for 300 000 events, yielding 930 cross-section values with an uncertainty in absolute normalization of ±4%. Only the $K^+$ and proton data show any significant change in slope of the forward diffraction peak with incident momentum. The particle-antiparticle crossover positions are consistent with no energy dependence, average values being 0.14 ± 0.03, 0.190 ± 0.006, and 0.162 ± 0.004 GeV$^2$ for $\pi$'s, $K$'s, and protons, respectively; these errors reflect both statistics and the ±1.5% uncertainty in particle-antiparticle relative normalization. Differences between particle and antiparticle cross sections isolate interference terms between amplitudes of opposite $C$ parity in the $t$ channel; these differences indicate that the imaginary part of the odd-$C$ nonflip-helicity amplitude has a $J_0(r(-t)^{1/2})$ structure for $-t < 0.8$ GeV$^2$, as predicted by strong absorption models. The cross-section differences for $K^{\pm}$ and proton-antiproton are in qualitative agreement with the predictions of $\omega$ universality, the agreement improving with increasing energy. The corresponding quark-model predictions relating the $\pi^{\pm}$ and $K^{\pm}$ differences failed by more than a factor of 2. We have combined our $\pi^{\pm}$ cross sections with other data to better determine the $\pi N$ amplitudes in a model-independent way; results of this analysis are presented.

## I. INTRODUCTION

Elastic scattering of elementary particles is a most fundamental process. At high energies such scattering is dominated by diffraction and is related to the inelastic processes through unitarity; in $t$-channel language this is usually described as Pomeron exchange. At intermediate energies, quantum-number-exchange amplitudes are also present and are often parameterized in terms of Regge-pole exchange.

Some of these latter amplitudes can be obtained by a careful comparison of similar reactions related by simple, well-defined symmetries. For example, the difference between particle and antiparticle elastic scattering from protons results from a sign change in the interference between even and odd $C$-parity exchanges in the $t$ channel. Near the forward direction the dominant even-$C$ amplitude is the imaginary helicity-nonflip amplitude, and the interference between it and the odd-$C$ amplitude can be used to study the imaginary nonflip part of the odd-$C$ exchange amplitude. This amplitude is often taken to be $\rho$ exchange in the case of $\pi p$ scattering and $\omega$ exchange for $Kp$ and $pp$ scattering.

The experimental particle-antiparticle differences can be compared with the expectations of various models. Such a comparison was made by Davier and Harari[1] for $K^{\pm}p$ scattering at 5 GeV/$c$; they found the amplitude to be consistent with the $J_0(r(-t)^{1/2})$ structure predicted by the dual absorption model. In the case of $\pi^{\pm}p$ scattering, detailed amplitude analyses have been made[2–5]; the pion